THE UNIVERSITY *of* EDINBURGH

Edinburgh Research Explorer

Modeling continuous source distributions in wave-based virtual acoustics

OPEN ACCESS

Modeling Continuous Source Distributions in Wave-based Virtual Acoustics

Stefan Bilbao[1] and Jens Ahrens[2]

[1] *Acoustics and Audio Group/Reid School of Music, University of Edinburgh, 12 Nicolson Square, Edinburgh, EH8 9DF, United Kingdom*

[2] *Audio Technology Group, Division of Applied Acoustics, Chalmers University of Technology, 412 96 Gothenburg, Sweden*

All acoustic sources are of finite spatial extent. In volumetric wave-based simulation approaches (including, e.g., the finite difference time domain method among many others), a direct approach is to represent such continuous source distributions in terms of a collection of point like sources at grid locations. Such a representation requires interpolation over the grid, and leads to common staircasing effects, particularly under rotation or translation of the distribution. In this article, a different representation is shown, based on a spherical harmonic representation of a given distribution. The source itself is decoupled from any particular arrangement of grid points, and is compactly represented as a series of filter responses used to drive a canonical set of source terms, each activating a given spherical harmonic directivity pattern. Such filter responses are derived for a variety of commonly-encountered distributions. Simulation results are presented, illustrating various features of such a representation, including convergence, behaviour under rotation, the extension to the time varying case and differences in computational cost relative to standard grid-based source representations.

[http://dx.doi.org(DOI number)]

[XYZ]   Pages: 1–13

I. INTRODUCTION

The emulation of sources in time domain wave-based virtual and architectural acoustics (such as the finite difference time domain method or FDTD[1–3], finite volume methods[4,5], finite element methods[6] and other varieties[7]) has a long history[8–13], and follows even earlier work on the representation of sources in electromagnetic simulation[14]. Time domain volumetric wave-based method, operating over a full 3D spatial grid are the focus here, though frequency-domain wave-based methods employing sources have also been proposed using boundary element techniques[15,16].

The implementation of sources with directivity in time domain wave-based acoustics has been explored by various authors. One approach involves combinations of a small number of basic sources, usually in alignment with a Cartesian grid, in order to generate simple directivity patterns[12,17]. Larger collections of simple monopole sources have been used as the basis for fitting against measured source directivities[18–20]. Source directivity modeling using spherical harmonic representations has been also been employed in wave-based methods, using pseudospectral time domain methods[7], and using FDTD[21], leading to a very sparse representation

of the source in terms of a canonical set of spherical harmonic difference operators and low order finite impulse response filters. Source directivity modeling in frequency domain wave-based methods has also been explored using the boundary element method[16] and equivalent source methods[15]; in this article, purely local time-domain wave-based simulation is addressed. Source modeling in wave-based methods is closely related to the problem of receiver modeling, which has also been approached using spherical harmonic representations, using BEM[15] and FDTD[22].

In this article, rather than focusing on fitting to measured source directivity, a model-based approach is taken in order to incorporate sources of distributed type, where the source is characterised as a continuous distribution of finite extent, assumed acoustically transparent. The motivation, in the context of virtual acoustics, is to allow the simulation of spatially-distributed sources when measurements are not available. An example is loudspeaker modeling, where pistons of finite size are the key element. Such distributed models are used extensively to model focusing effects in transducers in ultrasound[23–27] and aeroacoustics[28]. In such work, the distribution is represented directly in terms of simple sources defined over a grid; staircasing issues become a major concern, and one possible remedy is through the use of spectral collocation techniques[25,27], and direct approximation to the distribution in the wavenumber domain. Here, in the interest of a reduced representation that is flexible, particularly under translation and rotation, a spherical

harmonic formulation is employed, allowing the condensation of an arbitrary source distribution to a point-like directional source that can be implemented directly in the time domain. Such an approach follows from a time-dependent multipole representation[29], and is related to the multipole moment condensation method[30].
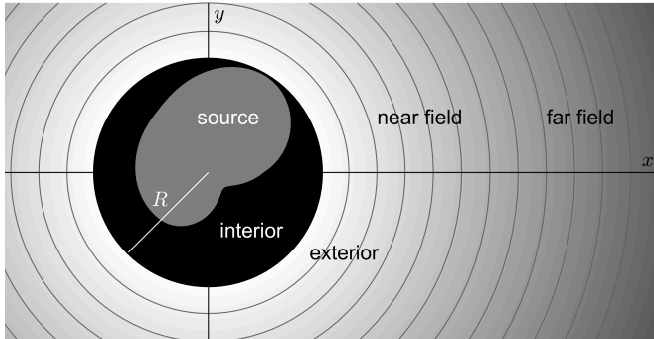

FIG. 1. A source distribution, inscribed within a sphere of radius R (illustrated in 2D here).

Point source models with arbitrary frequency-dependent directivity, and framed in terms of a time domain partial differential equation, are introduced in Section II. The extension to the case of continuous distributions of sources follows in Section III, leading to a compact formulation suitable for direct time domain discretisation. Representations of a variety of basic geometric source distributions are provided, in the interest of developing a library of low-complexity distributed source types that can be easily inserted into a wave-based time domain method regardless of the particular numerical method. Time domain discretisation, through FDTD methods is described in Section IV. Numerical results, illustrating comparisons against exact solutions, convergence with spherical harmonic order, frequency-dependent directivity, and rotations (including the time varying case) are presented in Section V. Some concluding remarks and perspectives appear in Section VI.

II. POINT SOURCE MODELS

A natural starting point is the 3D acousic wave equation including a monopole point source:

$$\frac{1}{c^2}\partial_t^2 p - \Delta p = f(t)\delta^{(3)}(\mathbf{r}) . \tag{1}$$

Here, $p(\mathbf{r}, t)$ is the acoustic pressure in Pa as a function of coordinate $\mathbf{r} = [x, y, z] \in \mathcal{D} \subseteq \mathbb{R}^3$ in m and time $t \in \mathbb{R}$ in s. c is the wave speed in m·s^{-1}, and $\Delta = \nabla \cdot \nabla$ is the 3D Laplacian, defined in terms of the gradient operator ∇

$$\nabla = [\partial_x, \partial_y, \partial_z] , \tag{2}$$

where $\partial_x, \partial_y, \partial_z$ represent partial differentiation with respect to x, y and z, respectively. $f(t)$ is a source strength with units kg· s^{-2}, and is causal, so that $f(t) = 0$ for

$t < 0$. The source is assumed to act pointwise at location $\mathbf{r} = \mathbf{0}$, through a 3D Dirac delta function $\delta^{(3)}(\mathbf{r})$ in (1) above[31]. In the rest of this article, the domain is assumed infinite, so $\mathcal{D} = \mathbb{R}^3$. The system is assumed defined for all time, so that initial conditions need not be supplied (though in simulation, they are assumed quiescent).

The solution to (1) may be written directly as

$$p(\mathbf{r}, t) = \frac{f(t - r/c)}{4\pi r} , \tag{3}$$

where $r = |\mathbf{r}|$. Under Fourier transformation, defined, for $p(\mathbf{r}, t)$, as

$$\hat{p}(\mathbf{r}, \omega) = \int_{-\infty}^{\infty} p(\mathbf{r}, t)e^{i\omega t}dt \tag{4}$$

for angular frequency ω in rad.· s^{-1}, the solution (3) transforms to

$$\hat{p}(\mathbf{r}, \omega) = \frac{\hat{f}e^{i\omega r/c}}{4\pi r} , \tag{5}$$

where $\hat{f}(\omega)$ is the Fourier transform of $f(t)$. Note the sign convention[32] in the definition of the Fourier transform in (4).

A. Pointwise Directional Source

Consider first the real orthonormal spherical harmonic functions $Y_{l,m}$ for $l \geq 0$ and $-l \leq m \leq l$. Here, one may write $Y_{l,m} = Y_{l,m}(\boldsymbol{\eta})$ in terms of a unit-length Cartesian three-vector $\boldsymbol{\eta} = [\eta_x, \eta_y, \eta_z]$. See Appendix A. $Y_{l,m}$ is a homogeneous polynomial of degree l and associated spatial partial differential operators $D_{l,m}$ are defined[21], for $l \geq 0$ and $-l \leq m \leq l$, as

$$D_{l,m} = Y_{l,m}(\nabla) . \tag{6}$$

These partial differential operators in ∂_x, ∂_y and ∂_z are homogeneous polynomials of degree l.

A time domain model of a point source centered at $\mathbf{r} = \mathbf{0}$ with arbitrary directivity may be written[21] as

$$\frac{1}{c^2}\partial_t^2 p - \Delta p = \sum_{l=0}^{\infty} \sum_{m=-l}^{l} b_{l,m}(t)D_{l,m}\delta^{(3)}(\mathbf{r}) , \tag{7}$$

where here, the signals $b_{l,m}(t)$ are related to an underlying source signal $f(t)$ by

$$b_{l,m}(t) = c^l(a_{l,m} * f)(t) . \tag{8}$$

Here, $*$ represents the continuous time convolution operation, and $a_{l,m}(t)$ is a filter response, assumed known.

The solution to (7) may be written, in the frequency domain, as

$$\hat{p} = \frac{i\omega}{4\pi c}\hat{f}\sum_{l=0}^{\infty} \sum_{m=-l}^{l} (-\omega)^l \hat{a}_{l,m}Y_{l,m}(\boldsymbol{\gamma}) h_l^{(1)}(\omega r/c) , \tag{9}$$

where here, $h_l^{(1)}$ is the lth spherical Hankel function of the first kind, and $\boldsymbol{\gamma} = \mathbf{r}/r$ is an angular 3-vector. $\hat{a}_{l,m}(\omega)$ is

the Fourier transform of $a_{l,m}(t)$. Thus the (l,m)th term in the model (7) encodes the contribution of the (l,m)th spherical harmonic to the source directivity, with $\hat{a}_{l,m}$ its frequency dependence.

The model described by (7) and (8) is the starting point for the modeling of distributed sources in the remainder of this article. It is framed entirely in the spatio-temporal domain, with the source defined point-wise, through the action of locally-defined Dirac distributions. This locality property has a number of important ramifications for any resulting numerical method. First, the computational cost of the source emulation remains very small in comparison with the computation of the field over the problem volume. Second, free space conditions are employed here, but the method is unchanged if a room geometry and wall conditions are supplied. It is also framed independently of the particular time domain numerical method to be used in its resolution; here, FDTD methods will be used, but any other method (FVTD, pseudospectral, or members of the finite element time domain family of methods such as spectral elements or discontinuous Galerkin methods) could be employed as well. Finally, due to the local spherical harmonic representation, operations such as rotation or translation of the source (even at run time) remain simple.

B. Displaced Point Source

When a monopole point source is displaced to $\mathbf{r} = \mathbf{r}_0$, the wave equation may be written as

$$\frac{1}{c^2}\partial_t^2 p - \Delta p = f(t)\delta^{(3)}\left(\mathbf{r} - \mathbf{r}_0\right) \qquad (10)$$

and the Fourier-transformed solution is

$$\hat{p}\left(\mathbf{r}, \omega\right) = \frac{\hat{f}e^{i\omega|\mathbf{r}-\mathbf{r}_0|/c}}{4\pi|\mathbf{r}-\mathbf{r}_0|}. \qquad (11)$$

Under an exterior expansion[33,34], one may arrive at the following representation for the acoustic field:

$$\hat{p} = \frac{i\omega\hat{f}}{c}\sum_{l=0}^{\infty}\sum_{m=-l}^{l} j_l\left(\frac{\omega r_0}{c}\right)Y_{l,m}\left(\boldsymbol{\gamma}_0\right)h_l^{(1)}\left(\frac{\omega r}{c}\right)Y_{l,m}\left(\boldsymbol{\gamma}\right), \qquad (12)$$

where here, $r_0 = |\mathbf{r}_0|$ and $\boldsymbol{\gamma}_0 = \mathbf{r}_0/r_0$. This expansion is valid for $r \geq r_0$.

By association with the solution for the directional source centered at $\mathbf{r} = \mathbf{0}$, from (9), one may make the identification

$$\hat{a}_{l,m} = 4\pi\left(-1\right)^l Y_{l,m}\left(\boldsymbol{\gamma}_0\right)\frac{j_l\left(\omega r_0/c\right)}{\omega^l}. \qquad (13)$$

In this simple case of a displaced point source, the time domain filter responses $a_{l,m}(t)$ are piecewise polynomial functions of t[21]. More importantly for wave-based simulation, they have finite support:

$$a_{l,m}(t) = 0 \qquad \text{when} \qquad |t| > r_0/c. \qquad (14)$$

For small r_0/c, and at audio sample rates, this implies that only short FIR filter designs will be required in implementation. The responses $a_{l,m}(t)$ are non-causal, reflecting the translation of the displaced source to a driving term at $\mathbf{r} = \mathbf{0}$.

III. DISTRIBUTIONS AND EXAMPLES

Consider now the extension of the point source model to a distribution $g(\mathbf{r})$, in units of m^{-3}:

$$\frac{1}{c^2}\partial_t^2 p - \Delta p = f(t)g(\mathbf{r}). \qquad (15)$$

Let us also assume that the distribution is spatially confined, so that a distance R is the smallest such that

$$g(\mathbf{r}) = 0, \qquad r \geq R. \qquad (16)$$

$g(\mathbf{r})$ is constrained to be real here, and it may, for convenience, be assumed to be normalized in some situations—see (23). See Figure 1. More generally, the right hand side of (15) could be replaced by a term $g(\mathbf{r}, t)$, but the separated form above captures many situations of interest[26]. Using the spherical harmonic representation of the point source from (12), one may integrate over the distribution $g(\mathbf{r})$ to yield

$$\hat{p} = \iiint_{\mathbb{R}^3} g(\mathbf{r}')\frac{i\omega\hat{f}}{c}\sum_{l=0}^{\infty}\sum_{m=-l}^{l} j_l\left(\frac{\omega r'}{c}\right)Y_{l,m}\left(\boldsymbol{\gamma}'\right)h_l^{(1)}\left(\frac{\omega r}{c}\right)Y_{l,m}\left(\boldsymbol{\gamma}\right)dV'. \qquad (17)$$

This gives, finally,

$$\hat{p} = \frac{i\omega\hat{f}}{c}\sum_{l=0}^{\infty}\sum_{m=-l}^{l} h_l^{(1)}\left(\omega r/c\right)Y_{l,m}\left(\boldsymbol{\gamma}\right)Q_{l,m}(\omega), \qquad (18)$$

where

$$Q_{l,m}(\omega) = \iiint_{\mathbb{R}^3} j_l\left(\omega r'/c\right)Y_{l,m}\left(\boldsymbol{\gamma}'\right)g\left(\mathbf{r}'\right)dV'. \qquad (19)$$

The $Q_{l,m}$ are exactly the multipole moments as defined by Heyman[29].

By association with the directional point source expansion, from (9), one has, for the filters $\hat{a}_{l,m}(\omega)$,

$$\hat{a}_{l,m}(\omega) = 4\pi\left(-\omega\right)^{-l}Q_{l,m}(\omega). \qquad (20)$$

Note that these filters are well-behaved in the limit as $\omega \to 0$ because $j_l\left(\omega r'/c\right) \propto \omega^l$ in this limit, and thus $Q_{l,m}(\omega) \propto \omega^l$. They also lead to time-limited responses, following from the case of the displaced point source, from (14), so that

$$a_{l,m}(t) = 0 \qquad \text{when} \qquad |t| > R/c. \qquad (21)$$

In implementation, these are most naturally realised as short FIR filters that entirely encapsulate the directivity properties of a given source distribution.

For easy reference, a variety of basic distributions $g(\mathbf{r})$, alongside the resulting function $Q_{l,m}(\omega)$ is given in

Figure 2. In this figure, $\delta^{(1)}$ and $\delta^{(2)}$ represent 1- and 2-dimensional Dirac delta functions, $_p\tilde{F}_q$ is the regularized hypergeometric function, and the box function $\sqcap(\zeta)$ is defined by
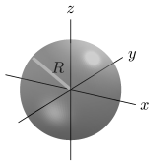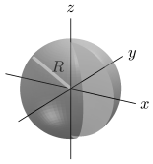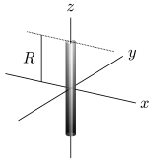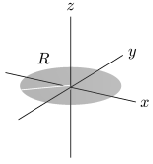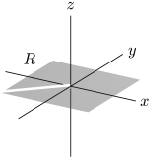
$$\sqcap(\zeta) = \begin{cases} 1, & |\zeta| \leq 1 \\ 0, & |\zeta| > 1 \end{cases}. \tag{22}$$

For convenience, all distributions $g(\mathbf{r})$ in the figure are assumed normalised, so that

$$\iiint_{\mathbb{R}^3} g(\mathbf{r}')dV' = 1. \tag{23}$$

This normalisation is neither necessary, nor even always possible (e.g., for distributions that are zero mean, such as the planar dipole distributions as described in Section III D). When normalised, however, the functions $Q_{l,m}$ may be written in terms of a dimensionless argument $\xi = \omega R/c$, and thus need only be computed once per geometry, offline, to any desired accuracy.

FIG. 2. Normalised distributions $g(\mathbf{r})$ and associated functions $Q_{l,m}$, written in terms of the dimensionless variable $\xi = \omega R/c$.

	Solid Sphere $$g(\mathbf{r}) = \frac{3}{4\pi R^3} \sqcap\left(\frac{r}{R}\right)$$ $$Q_{0,0} = \frac{3}{\sqrt{4\pi}} \frac{j_1(\xi)}{\xi}$$
	Spherical Shell $$g(\mathbf{r}) = \frac{1}{4\pi R^2}\delta^{(1)}(r - R)$$ $$Q_{0,0} = \frac{1}{\sqrt{4\pi}}j_0(\xi)$$
	Line Source $$g(\mathbf{r}) = \frac{1}{2R}\delta^{(2)}(x,y)\sqcap\left(\frac{z}{R}\right)$$ $$Q_{l,0} = \frac{l!\sqrt{(2l+1)\pi}}{2^{2l+3}(l/2)!}\xi^l {}_1\tilde{F}_2\left(\frac{1+l}{2};\frac{2l+3}{2};\frac{3+l}{2};-\frac{\xi^2}{4}\right)$$
	Disk $$g(\mathbf{r}) = \frac{1}{\pi R^2}\delta^{(1)}(z)\sqcap\left(\sqrt{x^2+y^2}/R\right)$$ $$Q_{l,0} = \frac{l!\sqrt{(2l+1)}i^l}{2^{2l+2}(l/2)!}\xi^l {}_1\tilde{F}_2\left(\frac{2+l}{2};\frac{2l+3}{2};\frac{4+l}{2};-\frac{\xi^2}{4}\right)$$
	Square $$g(\mathbf{r}) = \frac{1}{2R^2}\delta^{(1)}(z)\sqcap\left(\frac{x}{R}\right)\sqcap\left(\frac{y}{R}\right)$$ $$Q_{l,m} \neq 0 \quad \text{for } l \text{ even}, m \geq 0, \bmod(m,4) = 0$$

A. Spherically Symmetric Sources

Spherically symmetric source distributions, with $g(\mathbf{r}) = g(r)$ have a trivial representation in terms of the monopole component only, so that $Q_{l,m}$ vanishes except when $l = m = 0$. Indeed, (19) reduces to

$$Q_{0,0} = \sqrt{4\pi} \int_0^R j_0\left(\omega r'/c\right) g(r') \left(r'\right)^2 dr'. \tag{24}$$

Some basic configurations, illustrated in Figure 2, include a filled sphere and a hollow spherical shell. The distributions $g(\mathbf{r})$ and the resulting functions $Q_{l,m}(\omega)$ are given in the figure.

B. Line Source

For a line source, oriented with the z axis, and of length $2R$, and centered at $\mathbf{r} = \mathbf{0}$, $Q_{l,m}$ is non-zero for $m = 0$ and even l, and reduces to

$$Q_{l,0}(\omega) = \frac{1}{2R}\sqrt{\frac{2l+1}{4\pi}} \int_{-R}^R j_l\left(\omega z'/c\right) dz'. \tag{25}$$

This may be evaluated in terms of the regularized hypergeometric function, as in Figure 2.

C. Planar Monopole Sources

For a source distribution that is planar, and that lies in the $z = 0$ plane, the distribution $g(\mathbf{r})$ is of the form

$$g(\mathbf{r}) = \delta^{(1)}(z)g_0(x,y) \quad \text{for} \quad \iint_{\mathbb{R}^2} g_0(x',y')dx'dy' = 1, \tag{26}$$

where $\delta^{(1)}$ is a 1D Dirac delta function, and g_0 is a 2D distribution, with units m^{-2} and of maximal spatial extent R. Now, $Q_{l,m}$ reduces to

$$Q_{l,m} = \iint_{\mathbb{R}^2} j_l\left(\omega r'/c\right) Y_{l,m}\left(\gamma'\right) g_0 dx'dy'. \tag{27}$$

Here, the spherical harmonic functions $Y_{l,m}(\gamma)$ are evaluated for $z = 0$, as such, the integral above vanishes except when l and m are either both even or both odd. For geometries with more symmetry, additional terms vanish. For the special case of the circular disk all terms vanish unless l is even and $m = 0$, and expressions for $Q_{l,m}$ are available in closed form. For the case of a square region aligned with the coordinate axes, $Q_{l,m}$ is not available in closed form, but all terms vanish unless l is even and m is a non-negative multiple of 4. See Figure 2.

D. Dipole Source Distributions

A solution for the case of a dipole source distribution follows from the case of the source distribution under differentiation. Setting

$$g^{(d)}(\mathbf{r}) = -R\partial_z g(\mathbf{r}) \tag{28}$$

for a given distribution $g(\mathbf{r})$ gives a dipole distribution oriented with the z axis. It is possible to write the functions $Q_{l,m}^{(d)}$ in terms of $Q_{l,m}$ calculated for the distribution from (27), as

$$Q_{l,m}^{(d)} = \frac{R\omega}{c}\left(-\kappa_{l,m}^{+}Q_{l+1,m} + \kappa_{l,m}^{-}Q_{l-1,m}\right), \quad (29)$$

where

$$\kappa_{l,m}^{+} = \sqrt{\frac{(l+1)^2 - m^2}{(2l+1)(2l+3)}} \quad \kappa_{l,m}^{-} = \sqrt{\frac{l^2 - m^2}{4l^2 - 1}}. \quad (30)$$

Particular cases of interest are circular and square pistons derived from a planar distribution $g_0(x, y)$ where, in this case,

$$g^{(d)}(\mathbf{r}) = -R\partial_z\left(\delta^{(1)}(z)\right)g_0(x, y). \quad (31)$$

E. Rotations

The spherical harmonic representation lends itself very naturally to rotations of source distributions, normally specified in terms of three Euler angles (α, β, ψ); here, the standard 'zyz' convention is employed.

A function $\tilde{Y}_{l,m}$, a rotated spherical harmonic, may be written as a linear combination of unrotated spherical harmonic functions $Y_{l,m}$ of the same order l as

$$\tilde{Y}_{l,m} = \sum_{m=-l}^{l} \zeta_{l,m}(\alpha, \beta, \psi) Y_{l,m} \quad (32)$$

for some coefficients $\zeta_{l,m}(\alpha, \beta, \psi)$[35]. It then follows that an associated rotated differential operator $\tilde{D}_{l,m}$ may be defined as

$$\tilde{D}_{l,m} = \tilde{Y}_{l,m}(\nabla) \quad (33)$$

and remains a homogeneous spatial differential operator of degree l. The complete system corresponding to a rotated source distribution is then, from (7),

$$\frac{1}{c^2}\partial_t^2 p - \Delta p = \sum_{l=0}^{\infty}\sum_{m=-l}^{l} b_{l,m}(t)\tilde{D}_{l,m}\delta^{(3)}(\mathbf{r}). \quad (34)$$

This has important computational ramifications. In particular, for a given source distribution $g(\mathbf{r})$, the spherical harmonic filter kernels $a_{l,m}(t)$ (from which $b_{l,m}(t)$ above are derived) need only be computed once, and can thus be reused under any rotation. Furthermore, if, due to symmetry, only a reduced set of spherical harmonics is necessary to represent a given source distribution, this sparsity of the representation persists under rotation. All that is necessary is to compute a discrete approximation to the products $\tilde{D}_{l,m}\delta^{(3)}(\mathbf{r})$, which are independent of any particular source distribution. See Section V C for an illustration of simulation results for rotated distributions. It is direct to extend the rotation (32) to the time varying case through the use of time varying coefficients $\zeta_{l,m}(\alpha(t), \beta(t), \psi(t))$. See Section V D for an illustration of simulation results for the time-varying rotation of a circular piston.

IV. FDTD METHODS

FDTD methods are defined over regular grid arrangements (such as Cartesian); they are perhaps the simplest of all time domain wave-based methods, and scale well in parallel hardware. FDTD is discussed here for the sake of simplicity; the methodology for the condensation of distributed source distributions to a series of spherical harmonic filter responses described in Section III is independent of the particular choice of method.

Two-step FDTD methods solving the wave equation are minimal in terms of memory usage, and may be designed to any desired order of accuracy, in both time and space[36,37]. (Note that such formal high order accuracy holds only in free space, and can be disturbed in the presence of numerical boundary conditions. But the related effect of low dispersion over the bulk of the problem interior persists, even when the domain is terminated.) All explicit schemes may be written in the form

$$p_{\mathbf{q}}^{n+1} = 2p_{\mathbf{q}}^{n} - p_{\mathbf{q}}^{n-1} + \lambda^2 \mathcal{L}_{\mathbf{q}}^{n}. \quad (35)$$

Here, $p_{\mathbf{q}}^{n}$ represents an approximation to $p(\mathbf{r}, t)$ at $\mathbf{r} = \mathbf{q}X$ and $t = nT$, for integer n and integer-valued vector $\mathbf{q} = [q_x, q_y, q_z]$, where X is the grid spacing, and T is the time step (and $f_s = 1/T$ is the sample rate). The Courant number λ is defined as $\lambda = cT/X$. $\mathcal{L}_{\mathbf{q}}^{n}$ is a scaled approximation to the Laplacian of p, defined by

$$\mathcal{L}_{\mathbf{q}}^{n} = \sum_{\nu=1}^{M} w_{\nu} \sum_{\mathbf{e} \in P(\mathbf{m}_{\nu})}\left(p_{\mathbf{q}+\mathbf{e}}^{n} - p_{\mathbf{q}}^{n}\right) \quad (36)$$

in terms of M basic shells of grid points surrounding the approximation center, a set of weights w_{ν} and non-negative integer-valued shell index 3-vectors $\mathbf{m}_{\nu}$, $\nu = 1, \ldots, M$. $P(\cdot)$ represents the set of all permutations of a 3 vector, including sign changes. Generally, for all such schemes, the Courant number λ will be bounded from above as $\lambda \leq \lambda_{\max}$, where $\lambda_{\max}$ depends on w_{ν} and $\mathbf{m}_{\nu}$.

In this article, a sixth order (in time and space) scheme will be used, namely one of the so-called diamond variety[36]. It is defined for $M = 6$, with index vectors $\mathbf{m}_{\nu}$ and weights w_{ν}, $\nu = 1, \ldots, 6$ given by

$$\begin{aligned}
\mathbf{m}_1 &= [1\ 0\ 0] & w_1 &= \tfrac{3}{2} - \tfrac{115}{72}\lambda^2 + \tfrac{41}{120}\lambda^4 \quad (37)\\
\mathbf{m}_2 &= [1\ 1\ 0] & w_2 &= \tfrac{5}{18}\lambda^2 - \tfrac{1}{10}\lambda^4\\
\mathbf{m}_3 &= [2\ 0\ 0] & w_3 &= -\tfrac{3}{20} + \tfrac{2}{9}\lambda^2 - \tfrac{1}{20}\lambda^4\\
\mathbf{m}_4 &= [1\ 1\ 1] & w_4 &= \tfrac{1}{60}\lambda^4\\
\mathbf{m}_5 &= [2\ 1\ 0] & w_5 &= -\tfrac{1}{72}\lambda^2 + \tfrac{1}{120}\lambda^4\\
\mathbf{m}_6 &= [3\ 0\ 0] & w_6 &= \tfrac{1}{90} - \tfrac{1}{72}\lambda^2 + \tfrac{1}{360}\lambda^4.
\end{aligned}$$

In this case, $\lambda_{\max} = 1/\sqrt{3}$. For a sample rate of 44.1 kHz, this particular scheme has a maximum phase velocity deviation of approximately 0.04% up to 4 kHz over all propagation directions[37], and requires access to a 61 point stencil of grid points surrounding the central grid point. See Figure 3.
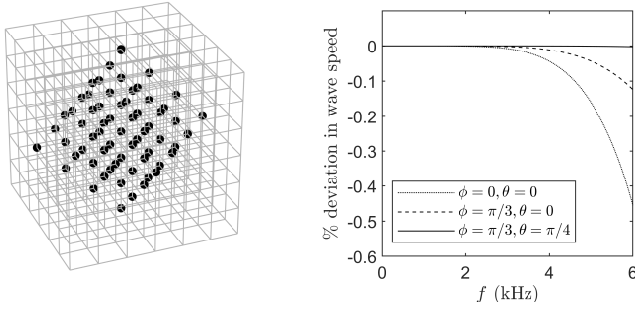
FIG. 3. Left: stencil for scheme (35), using the shell index vector set given in (37). Right: percentage error in phase velocity as a function of frequency, for the scheme running at 44.1 kHz, at directions as indicated.

A. Source Term: Direct Discretisation

A direct approach to discretisation of the model (15) follows from sampling of the input signal $f(t)$, yielding a discrete time signal f^n, and through a discrete representation of the distribution $g(\mathbf{r})$, yielding a grid function $g_{\mathbf{q}}$. The resulting scheme is of the form:

$$p_{\mathbf{q}}^{n+1} = 2p_{\mathbf{q}}^n - p_{\mathbf{q}}^{n-1} + \lambda^2 \mathcal{L}_{\mathbf{q}}^n + T^2 f^n g_{\mathbf{q}}. \qquad (38)$$

There are many approaches to deriving $g_{\mathbf{q}}$ from $g(\mathbf{r})$. The simplest, available in a limited number of settings, is a direct "on grid" sampling, suitable when the source distribution is aligned with an underlying grid. For the cases of the filled sphere and line source illustrated in Figure 4, the most basic possible discrete representation (a binary mask) is used. This simple approach leads to an incorrect approximation to the volume (resp. length) of the source, and ultimately to deviations in computed responses from exact solutions. See, e.g., Section V A for an illustration of such errors. More elaborate strategies involve the introduction of scaling factors[24], and can cope with this issue. Another possibility is to represent a distribution in terms of a collection of off-grid source points, then distributed to the grid via interpolation (perhaps bandlimited[38]). A similar idea of bandlimited point source representations has appeared in the context of off-grid sources in virtual acoustics[39]. The deeper problem is that such an approach ultimately requires starting from scratch for each new orientation of the source relative to the grid, and introduces new choices for the user to make (e.g., the arrangement/density of off-grid sources). On the other hand, it is capable of reproducing effects in the extreme near vicinity of the distribution. It is not the intention in this article to explore the many varieties of such approximation strategies, and only basic on-grid approximations will be used here for comparison in some cases.
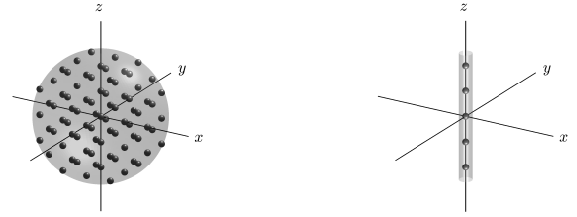

FIG. 4. On grid discretisations of a filled spherical distribution (left) and a line source (right).
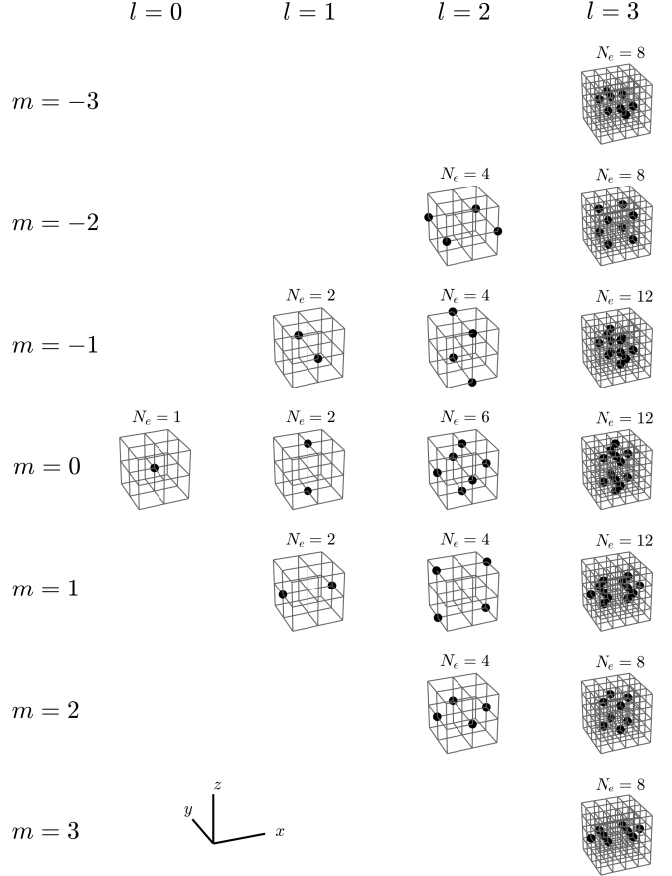
FIG. 5. Spatial patterns of grid functions $v_{l,m,\mathbf{q}}$, approximating $D_{l,m}\delta^{(3)}(\mathbf{r})$ using a basic centered difference approximation, for orders $l = 0, 1, 2, 3$. In each case the number N_e of non-zero elements is indicated.

B. Source Term: Discrete Spherical Harmonic Representation

The procedure for the discretisation of the spherical harmonic source model given in (7) relies upon the approximation of the Dirac delta function under the action of the differential operators $D_{l,m}$, as defined in (6). The approximation of the Dirac function and its derivatives over a grid has been approached by many authors[40–42]. Here the most simple forms of approximations using basic

centered differences are used, as described in a previous work[21]. Ultimately, grid functions

$$v_{l,m,\mathbf{q}} \cong D_{l,m}\delta^{(3)}(\mathbf{r}) \tag{39}$$

may be derived—see Figure 5, illustrating spatial pattern of the grid functions $v_{l,m,\mathbf{q}}$ up to order $l = 3$. Notice that these are sparse (with the number of non-zero entries indicated in the figure). The grid function $v_{l,m,\mathbf{q}}$ scales with $1/X^{l+3}$, and weightings for the various non-zero elements may be derived using a simple recursive procedure[21].

A complete discretisation of (7) then follows as

$$p_{\mathbf{q}}^{n+1} = 2p_{\mathbf{q}}^n - p_{\mathbf{q}}^{n-1} + \lambda^2 \mathcal{L}_{\mathbf{q}}^n + c^2 T^2 \sum_{l=0}^{\infty} \sum_{m=-l}^{l} b_{l,m}^n v_{l,m,\mathbf{q}} \cdot \tag{40}$$

The signals $b_{l,m}^n$ are obtained through discrete time convolution of the source signal f^n with $a_{l,m}^n$, in analogy with (8). No additional numerical stability considerations arise, as the model above does not incorporate any feedback terms. Under a rotation of the source distribution (see Section III E), the grid functions will be replaced by $\tilde{v}_{l,m,\mathbf{q}}$, defined by

$$\tilde{v}_{l,m,\mathbf{q}} = \sum_{m=-l}^{l} \zeta_{l,m}(\alpha,\beta,\psi) v_{l,m,\mathbf{q}}. \tag{41}$$

Note that because there is considerable overlap over the sets of grid points over which the $v_{l,m,\mathbf{q}}$ are defined, for a given order l, the grid functions $\tilde{v}_{l,m,\mathbf{q}}$ exhibit roughly the same sparsity as $v_{l,m,\mathbf{q}}$.

The complete form of scheme (40) in implementation is most easily seen in a vector-matrix update form. Consider the case of a maximal spherical harmonic order of $l = L$. Consolidating the entire grid function $p_{\mathbf{q}}^n$ into a vector of the form $\mathbf{p}^n$, the two-step update takes the form

$$\mathbf{p}^{n+1} = 2\mathbf{p}^n - \mathbf{p}^{n-1} + \lambda^2 \mathbf{l}^n + c^2 T^2 \mathbf{V} \mathbf{b}^n. \tag{42}$$

Here, $\mathbf{l}$ is a vector representing the scaled Laplacian operation $\mathcal{L}_{\mathbf{q}}$ applied to $p_{\mathbf{q}}^n$ from (36), and $\mathbf{V}$ and $\mathbf{b}$ are defined by

$$\mathbf{V} = [\mathbf{v}_{0,0} \ \mathbf{v}_{1,-1} \ \ldots \ \mathbf{v}_{L,L}] \quad \mathbf{b}^n = [b_{0,0}^n \ b_{1,-1}^n \ \ldots b_{L,L}^n]^T. \tag{43}$$

$\mathbf{V}$ consists of $(L+1)^2$ column vectors $\mathbf{v}_{l,m}$, which are in general extremely sparse. Depending on the symmetry of the source distribution, it may not be necessary to include all the spherical harmonic grid functions within $\mathbf{V}$—see Section III, and especially the case of spherically-symmetric distributions with only a single spherical harmonic component. This sparsity persists under any rotation, in which case the matrix $\mathbf{V}$ is replaced by $\tilde{\mathbf{V}}$, consisting of the concatenation of vectors $\tilde{\mathbf{v}}_{l,m}$ obtained through rotation of the vectors $\mathbf{v}_{l,m}$.

V. NUMERICAL EXAMPLES

All simulations are run using the sixth order accurate (in time and space) scheme given by (35), using shell index vectors and weights from (37). The sample rate is chosen as 44.1 kHz, and $\lambda = 1/\sqrt{3}$. Output is drawn from the scheme at locations that do not necessarily align with the grid, using 10th order separable bandlimited interpolants[39], allowing for effectively no additional error other than dispersion error, as illustrated in Figure 3. The computational domain is a cube of side length 2 m, and simulations are halted before reflections from the domain boundaries are recorded by receivers.

Input signals $f = f^n$ used are of the form of an impulse, in the case of directivity plots:

$$f^n = \begin{cases} 1, & n = 0 \\ 0, & n > 0 \end{cases}. \tag{44}$$

Gaussian signals of the form

$$f^n = \exp\left(-\frac{(nT - \tau_\epsilon)^2}{2\tau_0^2}\right) \tag{45}$$

are used for plots illustrating propagation and receiver signals. Here τ_0 is the RMS width, in s. So that the signal effectively starts at $n = 0$, the shift τ_ϵ may be chosen as $\tau_\epsilon = \tau_0\sqrt{-2\ln(\epsilon)}$ where ϵ represents machine epsilon in double precision floating point arithmetic.

The time series $b_{l,m}^n$ are obtained through discrete time convolution of the input time series f^n with the source encoding filters $a_{l,m}^n$. The $a_{l,m}^n$, in turn, are obtained offline from inverse Fourier transformation of $\hat{a}$ as defined in (20), at the prescribed sample rate; as mentioned earlier, the filters $a_{l,m}^n$ need only be determined once, regardless of the particular location or rotation of the source distribution, or the choice of numerical method.

Reference solutions used for comparison are generated either in the time domain, by integrating the free space solution (3) for a monopole or similarly in the frequency domain, for directivity plots, using (5), over the distribution at a very high resolution until convergence (in this case, to six decimal places) is reached.

A. Spherically Symmetric Sources

As a basic example, consider the case of spherically symmetric sources of the form of a filled ball and spherical shell, as illustrated in Figure 2. In Figure 6, output waveforms p_{out} are shown for distributions of varying radii R, alongside exact solutions that can be computed in closed form directly from (15) using, e.g., double Fourier inversion in space and time and inverse transformation to the spatiotemporal domain. The distributions are centered at $\mathbf{r} = \mathbf{0}$, and output is drawn from the location $\mathbf{r} = [0, 0, 0.3]$ m, and the input is a Gaussian signal of the form of (45), with $\sigma = 5 \times 10^{-5}$. Here, the spherical harmonic scheme (40) is employed, with a single term ($l = 0$, $m = 0$).
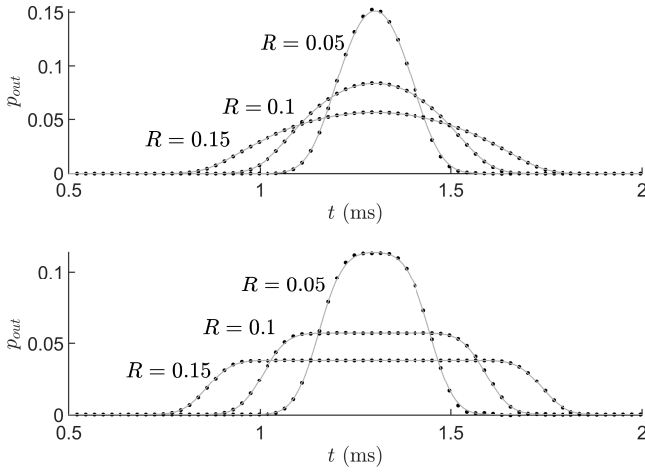
FIG. 6. Simulated pressure output waveforms (dots) and exact solution for simulations of the filled sphere (top) and spherical shell (bottom) distributions, for sphere radii R as indicated. The exact solution appears in solid grey.
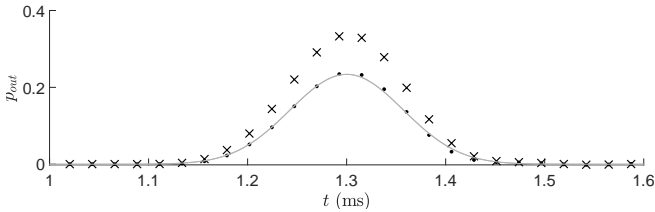

FIG. 7. Exact solution (grey solid line) and numerical solution computed using the spherical harmonic difference scheme (40) (dots) and using a coarse staircased approximation to a filled sphere (crosses).

In contrast, consider the case of the direct discretisation of the distribution, using scheme (38), and the most basic on-grid representation of the filled sphere, as shown in Figure 4. In this case, the output pressure is severely overestimated. See Figure 7, illustrating output waveforms using both the spherical harmonic representation and an on grid representation of the source, for a smaller filled sphere of radius $R = 0.02$ m, with other conditions the same as for Figure 6. The overestimation is in direct proportion to the effective volume of the discrete distribution, and will decrease as the sample rate is increased (and thus grid spacing is decreased). Compensating for this effect can be carried out by a variety of means, including the scaling of grid point weightings near the edge of the distribution, or more advanced off-grid methods (requiring more precomputation)[24,38]. In the spherical harmonic representation, the distribution volume is directly encoded in the filters $a_{l,m}$.

In terms of computational cost, the spherical harmonic representation requires, in this very simple case, a single filtering operation (FIR, with the kernel $a_{0,0}^n$, of duration $2f_s R/c$ samples) applied to the input sig-

nal, which is then inserted at a single grid point. In contrast, for the direct source discretisation, there is no filtering operation, but the number of grid points that must be operated upon scales with the volume. For larger source distributions, this can become heavy quickly: for $R = 0.15$ m, at a 44.1 kHz sample rate, a filled sphere includes 5449 points. In contrast, filter impulse response lengths scale linearly with the size R of the source. This advantage will persist for any source distribution that is most easily represented in 3D.

B. Time Domain Simulation Results and Convergence with Spherical Harmonic Order

In Figure 8, simulation results are shown using a Gaussian input signal, and for the line source, and square and circular distributions, as per Figure 2, as well as for circular and square dipole distributions, using the simple transformation of the multipole moments as given in (29). All have size $R = 0.1$ m, and output is taken in the near field at $r = 0.3$ m in different directions, as indicated. A maximal spherical harmonic order of $L = 10$ is used in this case. At this order, matches are nearly exact—visible, in the case of dipole distributions, are slight undershoots for wave propagation in the axial direction. This effect was pointed out in previous work[39], and is due to the choice of a simple centered difference approximation in order to form the vectors $\mathbf{v}_{l,m}$. One way to improve upon this is through the use of non-centered approximations (at the expense of a phase offset). Another is through approximations using wider sets of grid points to approximate the Dirac delta under various spherical harmonic differential operators. Such approximations can be optimised over an appropriate wavenumber range[39].

The question of convergence with maximal spherical harmonic order L is a large one; it depends strongly on the geometry of the distribution itself, but also on the frequency content of the input signal, as well as the distance to the receiver point (i.e., whether in the near field or far field). A clear worst case is the line source, as illustrated in Figure 9 at left; for distributions closer to spherical, such as the circular disk, convergence is much faster. For contrast, consider the worst case of the line source, under a direct discretisation, as per (38). Here, using a collection of unscaled on grid sources as shown in Figure 4. Time domain responses are again incorrect due to the misapproximation of the line source length, as shown in Figure 10, but easily fixed in this case using a simple scaling of weights at the endpoints of the line source. In this special case of a line source aligned with one of the grid axes, a direct discretisation approach is superior to the spherical harmonic representation with regard to both computational efficiency and accuracy, but once the line source is rotated or translated, then precomputation and runtime costs mount, and accuracy will decrease.
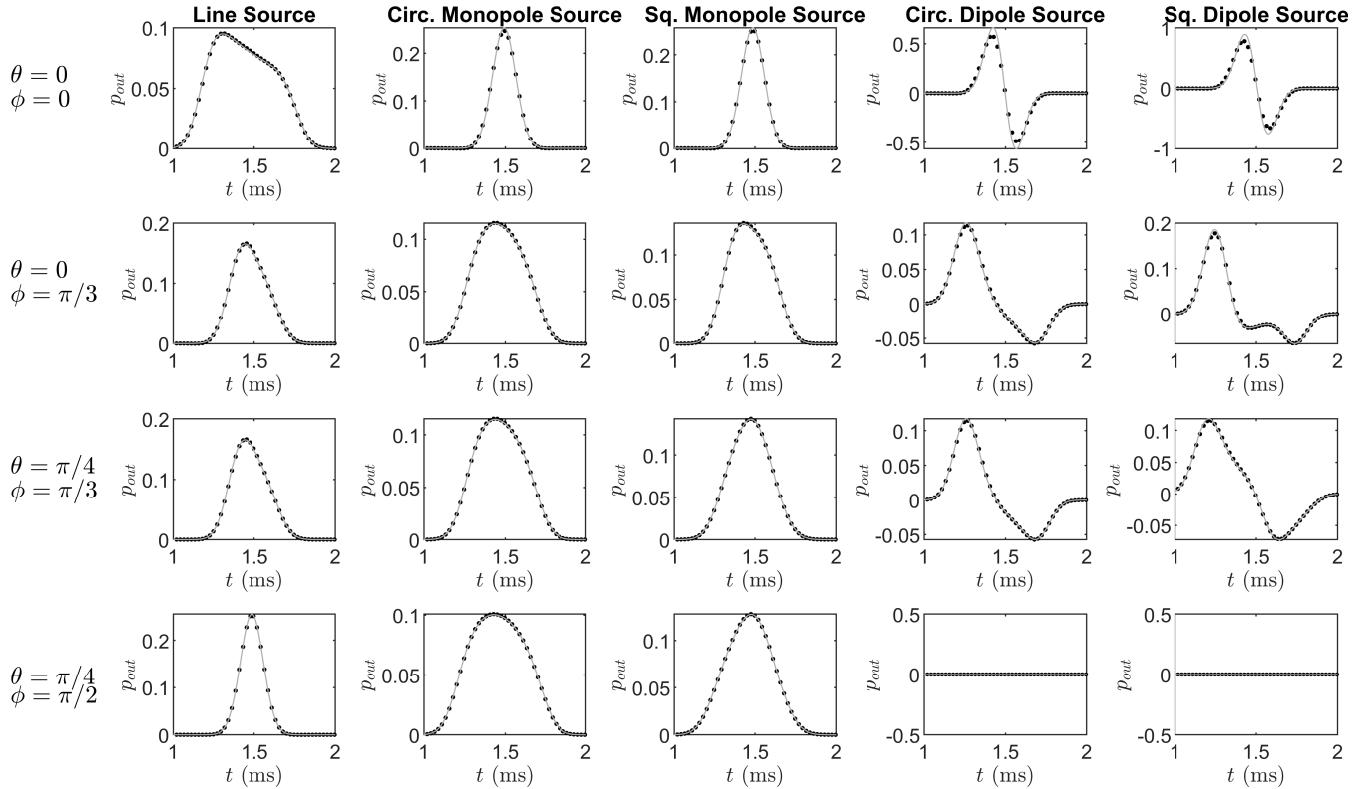
FIG. 8. Pressure waveforms drawn from scheme (40), for different source distributions, as indicated at the top of each column, and at different output locations, as indicated at left in each row, all at a distance $r = 0.3$ m from the source distribution center. All distributions have $R = 0.1$ m, and the input is a Gaussian signal with $\sigma = 7 \times 10^{-5}$. Reference outputs are shown in solid grey.

C. Directivities and Rotations

It is also useful to examine directivity patterns generated by various source distributions. See Figure 11 for balloon plots of normalized directivity for the line source, circular monopole disk and square dipole, all with $R = 0.1$ m, taken in the near field at $r = 0.3$ at different frequencies. Here, scheme (40) is used, with an impulse excitation (44), and using a maximal spherical harmonic order of $L = 10$. Time domain output is drawn using a spherical array of 1800 receivers (60 azimuthal × 30 in inclination), and then Fourier transformed.

Examples of directivities under rotation are illustrated in Figure 12; runtime computational cost is nearly identical to the case of the unrotated distributions.

D. Time-varying Rotations

One of the great advantages of working within a fully time domain framework is the ability to extend to the case of time varying sources at minimal additional computational cost. Time varying translations of sources have been examined in the FDTD framework in previous work[39], but may be extended to handle rotations of distributed sources as well.

As a basic example, consider a circular dipole distribution of radius 0.1 m, subject to an excitation consisting of a series of Gaussian impulses of the form of (45), with $\sigma = 4 \times 10^{-5}$. The disk is aligned initially with the z axis, and is rotated at a steady rate, over a period of 2.61 ms to an alignment with the x axis. This rate of rotation is unnaturally fast, but allows for a visualisation as shown in Figure 13. A 10th order spherical harmonic representation is used.

In terms of computational cost, the only operations to be performed here are the computation of the coefficients $\zeta_{l,m}^n$ at each time step, as a function of the current Euler angles, which is a simple recursive procedure[35] and the recombination of spherical harmonic grid functions $\mathbf{v}_{l,m}$ to form $\tilde{\mathbf{v}}_{l,m}^n$. Recall that the grid functions $\mathbf{v}_{l,m}$ are extremely sparse, with a small number of non-zero values clustered around the source grid point center. Furthermore, the vectors $\mathbf{v}_{l,m}$ can be precomputed once, independently of any particular source distribution or grid spacing.

VI. CONCLUDING REMARKS

The main contribution of this article has been to present an alternative representation of arbitrary source
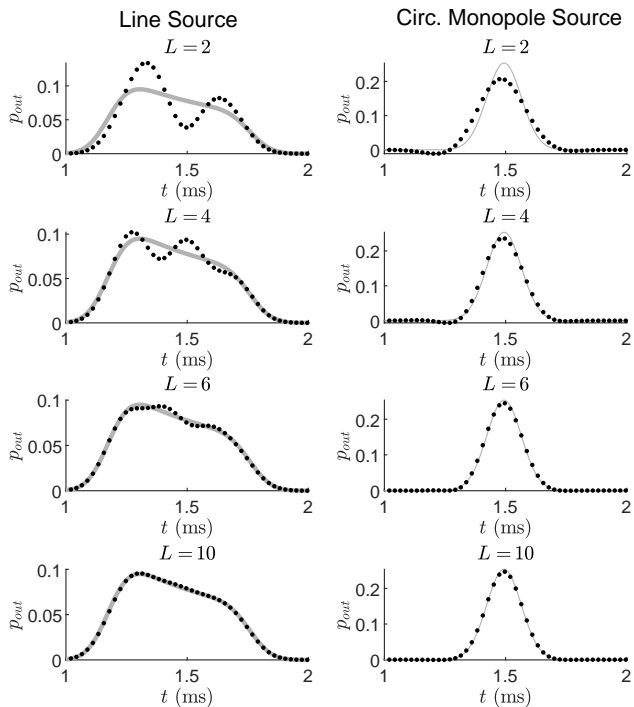
FIG. 9. Convergence of computed waveforms with maximal spherical harmonic order L in the case of the line source (left) and circular distribution (right). Output is taken on the positive z axis, at $r = 0.3$ m, and a Gaussian input signal with $\sigma = 4 \times 10^{-5}$ is used.
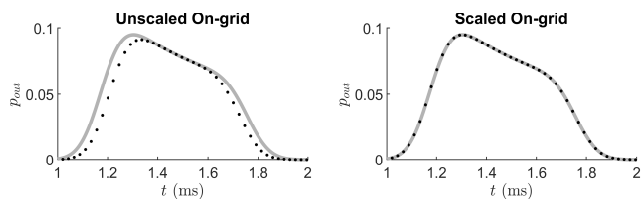

FIG. 10. Time domain waveforms generated for a line source, under the same conditions as for Figure 9, using a direct on grid discretisation, without scaling (left) and with scaling (right).
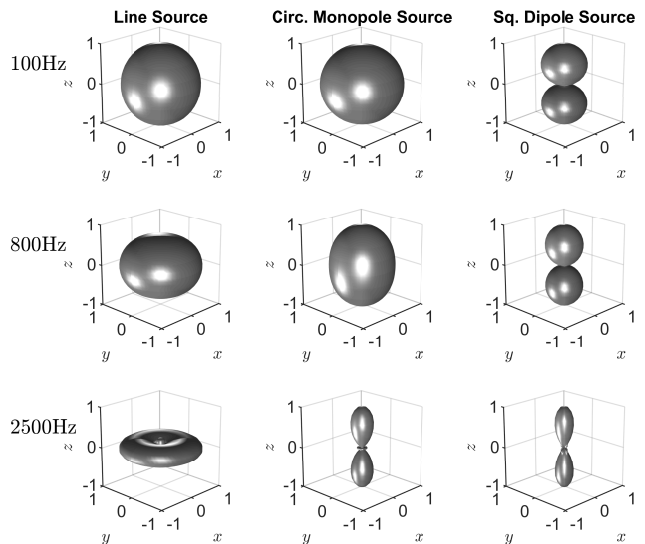

FIG. 11. Normalized directivity patterns for the line source (left), circular monopole disk (center) and square dipole source (right), at frequencies as indicated. All have $R = 0.1$ m.
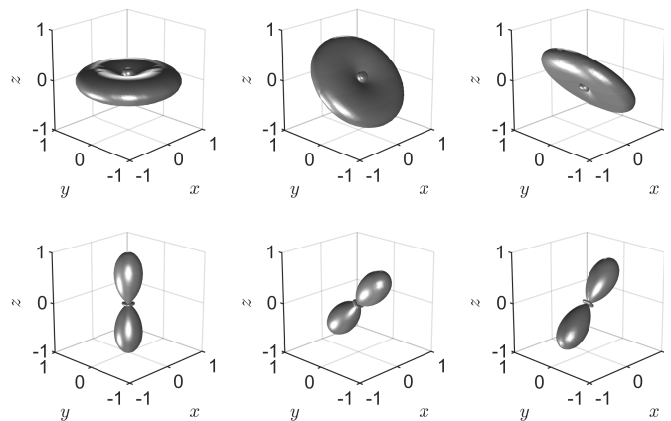
FIG. 12. Normalized directivity patterns for the line source (top row) and circular monopole disk (bottom row), both with $R = 0.1$ m, at 2500 Hz, and at a receiver distance of $r = 0.3$ m under different rotations. Left: unrotated. Center: under a rotation of $\pi/4$ about the y axis. Right: under a rotation of $\pi/4$ about the x axis.

distributions of finite spatial extent. The representation is framed purely in the spatiotemporal domain, and is thus suitable for direct discretisation in a time domain wave-based simulation method. Source distributions may be incorporated through an additional filtering step, with spherical harmonic channel filters derived directly from the source distribution. The main advantages of a spherical harmonic representation of a source distribution are its generality and flexibility.

With regard to generality, a given distribution may be characterised in the continuous domain, prior to any discretisation, and thus perhaps the most difficult part of the problem is shifted to a precomputation stage. As indicated, under a suitable normalisation of the source dis-

tribution, the precomputation need be carried out one time only for each separate geometrical configuration, and is scale invariant. This general mesh-free representation allows the sidestepping of staircasing problems that are inherent to representations of distributions over regular grids. Also, due to the locality of the source model, there is no spurious interaction of the source model with wall conditions. The spherical harmonic representation is limited, however, by its inability to represent the acoustic

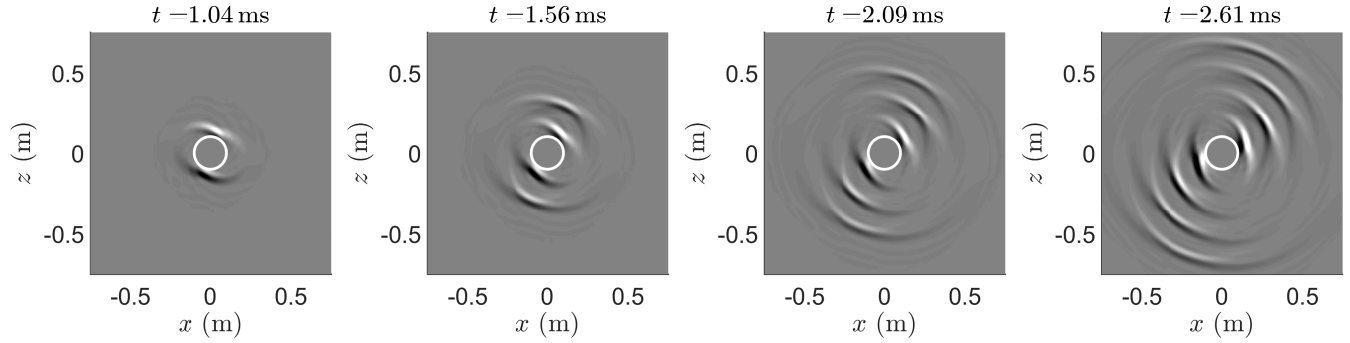FIG. 13. Snapshots of the time evolution of the acoustic field radiated by a circular dipole distribution, of radius $R = 0.1$ m, at times as indicated. At time $t = 0$, the disk is oriented with the positive z axis, and over the duration of the simulation (2.61 ms) is rotated to alignment with the positive x axis. A 10th order spherical harmonic representation is employed. The interior region over which the spherical harmonic representation is not valid is indicated by a white circle.

field over a region interior to the smallest sphere enclosing the distribution. In this sense, it is less general than an approach based on direct discretisation of a distribution. Not examined here is the case of phase variation over a given distribution which will be examined in future work.

With regard to flexibility, once the $a_{l,m}(t)$ spherical harmonic filter kernels are computed for a given source distribution, they may be used in any time domain numerical method directly, with FDTD used here as a simple example. It also becomes possible to perform rotations of the source, again avoiding staircasing artefacts, with minimal computational effort required in order to move to the time varying setting. Translations to off-grid source locations, if needed, are straightforward to implement through basic interpolation operators[39]. The representation in terms of short FIR filter responses is parsimonious, and even more so when the distribution exhibits symmetry.

Efficiency relative to a direct discretisation of a given distribution is a large question, and is highly problem specific; some comparisons have been made here in particular cases, however. It will depend strongly on the symmetry of the distribution and the extent to which source energy is concentrated in low spherical harmonic orders (thus allowing fast convergence), the alignment of the source with an underlying grid, on whether runtime performance is prioritised, whether sources are allowed to rotate during the course of a simulation, and other factors.

One aspect not discussed in this article is the behaviour of such source models in the presence of numerical dispersion, inherent to all volumetric wave-based time domain methods, and leading to perceptual artefacts[43]. Here, a high accuracy sixth order (in time and space) FDTD scheme has been used in order to minimize such effects, and concentrate on the core problem of the modeling of source distributions. In the case of source models, the analysis of dispersion is complicated by the fact that one must cope with not only the dispersion error of the numerical scheme (in isolation) but also the new error

introduced in the distinct approach to spatial discretisation of the source terms. Here, only the simplest possible local difference approximations to the source terms have been employed, but it is not difficult to imagine that one could do better with more advanced designs. The dual problem of the analysis of receiver designs in wave-based simulation methods, and the interaction with numerical dispersion has been discussed in various publications, in the context of spherical array designs designs[13], volumetric designs[44], as well as local SH receiver models similar to those proposed here for sources[22].

APPENDIX A: SPHERICAL HARMONICS IN CARTESIAN FORM

In this article, real orthonormal spherical harmonic functions are used in Cartesian form, and written in terms of the components of a unit length 3-vector $\boldsymbol{\eta} = [\eta_x, \eta_y, \eta_z]$. $Y_{l,m}(\boldsymbol{\eta})$ may be written explicitly, using $m = \bar{m}\sigma$, where $\bar{m} = |m|$ and $\sigma = \operatorname{sgn}(m)$, as

$$Y_{l,m}(\boldsymbol{\eta}) = \sqrt{\frac{(2l+1)(l-\bar{m})!(1+|\sigma|)}{2^{2l+2}\pi(l+\bar{m})!}}\,\bar{m}!G_{l,\bar{m}}H_m \quad \text{(A1)}$$

where

$$G_{l,\bar{m}} = \sum_{\nu=0}^{\lfloor\frac{l-\bar{m}}{2}\rfloor} \frac{(-1)^\nu (2l-2\nu)!\eta_z^{l-2\nu-\bar{m}}|\boldsymbol{\eta}|^{2\nu}}{\nu!(l-\nu)!(l-2\nu-\bar{m})!} \quad \text{(A2)}$$

$$H_m = \sum_{\nu=0}^{\bar{m}} \frac{\eta_x^\nu \eta_y^{\bar{m}-\nu}}{\nu!(\bar{m}-\nu)!} \cos\left(\frac{\pi(\bar{m}-\nu-\frac{|\sigma|}{2}(1-\sigma))}{2}\right) .\quad \text{(A3)}$$

Notice the factors of $|\boldsymbol{\eta}|^{2\nu} = 1$ in the definition of $G_{l,\bar{m}}$, which serve to render the polynomial $Y_{l,m}$ in (A1) homogeneous of degree l. See Table I for a representation of the spherical harmonic functions to third order.

[1]L. Savioja, T. Rinne, and T. Takala, "Simulation of room acoustics with a 3-D finite-difference mesh," in *Proc. Int. Comp. Music Conf.*, Århus, Denmark (1994), pp. 463–466.

TABLE I. Orthonormal real spherical harmonics $Y_{l,m}$ in Cartesian form, written in terms of the components of the unit-length vector $\boldsymbol{\eta} = [\eta_x, \eta_y, \eta_z]$ for $l = 0, 1, 2, 3$. Expressions in the table should be scaled by $\sqrt{1/4\pi}$.

$m\backslash l$	0	1	2	3
-3	$\cdot$	$\cdot$	$\cdot$	$\sqrt{\frac{35}{8}}\eta_y\left(3\eta_x^2 - \eta_y^2\right)$
-2	$\cdot$	$\cdot$	$\sqrt{15}\eta_x\eta_y$	$\sqrt{105}\eta_x\eta_y\eta_z$
-1	$\cdot$	$\sqrt{3}\eta_y$	$\sqrt{15}\eta_y\eta_z$	$\sqrt{\frac{21}{8}}\eta_y\left(4\eta_z^2 - \eta_x^2 - \eta_y^2\right)$
0	1	$\sqrt{3}\eta_z$	$\sqrt{\frac{5}{4}}\left(2\eta_z^2 - \eta_x^2 - \eta_y^2\right)$	$\sqrt{\frac{7}{4}}\eta_z\left(2\eta_z^2 - 3\eta_x^2 - 3\eta_y^2\right)$
1	$\cdot$	$\sqrt{3}\eta_x$	$\sqrt{15}\eta_x\eta_z$	$\sqrt{\frac{21}{8}}\eta_x\left(4\eta_z^2 - \eta_y^2 - \eta_x^2\right)$
2	$\cdot$	$\cdot$	$\sqrt{\frac{15}{4}}\left(\eta_x^2 - \eta_y^2\right)$	$\sqrt{\frac{105}{4}}\eta_z\left(\eta_x^2 - \eta_y^2\right)$
3	$\cdot$	$\cdot$	$\cdot$	$\sqrt{\frac{35}{8}}\eta_x\left(\eta_x^2 - 3\eta_y^2\right)$

[2] D. Botteldooren, "Acoustical finite-difference time-domain simulation in a quasi-Cartesian grid," J. Acoust. Soc. Am. **95**(5), 2313–2319 (1994).

[3] D. Botteldooren, "Finite-difference time-domain simulation of low-frequency room acoustic problems," J. Acoust. Soc. Am. **98**(6), 3302–3308 (1995).

[4] S. Bilbao, "Modeling of complex geometries and boundary conditions in finite difference/finite volume time domain room acoustics simulation," IEEE Trans. Audio Speech Language Proces. **21**(7), 1524–1533 (2013).

[5] S. Bilbao, B. Hamilton, J. Botts, and L. Savioja, "Finite volume time domain room acoustics simulation under general impedance boundary conditions," IEEE/ACM Trans. Audio Speech Language Proces. **24**(1), 161–173 (2016).

[6] T. Okuzono, T. Yoshida, K. Sakagami, and T. Otsuru, "An explicit time-domain finite element method for room acoustics simulations: Comparison of the performance with implicit methods," Appl. Acoust. **104**, 76–84 (2015).

[7] F. Georgiou and M. Hornikx, "Incorporating directivity in the Fourier pseudospectral time-domain method using spherical harmonics," J. Acoust. Soc. Am. **140**(2), 855–865 (2016).

[8] J. Schneider, C. Wagner, and S. Broschat, "Implementation of transparent sources embedded in acoustic finite-difference time domain grids," J. Acoust. Soc. Am. **103**(1), 3219–3226 (1998).

[9] A. Celestinos and S. Nielsen, "Low-frequency loudspeaker room simulation using finite differences in the time domain part 1: Analysis," J. Audio Eng. Soc. **56**(10), 772–786 (2008).

[10] J. Botts, A. Bockman, and N. Xiang, "On the selection and implementation of sources for finite-difference methods," in *Proc. 20th Int. Congr. Acoust.*, Sydney, Australia (2010).

[11] H. Jeong and Y. Lam, "Source implementation to eliminate low-frequency artifacts in finite difference time domain room acoustic simulation," J. Acoust. Soc. Am. **131**(1), 258–268 (2012).

[12] D. Murphy, A. Southern, and L. Savioja, "Source excitation strategies for obtaining impulse responses in finite difference time domain room acoustics simulation," Appl. Acoust. **82**, 6–14 (2014).

[13] J. Sheaffer, M. van Walstijn, and B. Fazenda, "Physical and numerical constraints in source modeling for finite difference simulation of room acoustics," J. Acoust. Soc. Am. **135**(1), 251–261 (2014).

[14] D. Buechler, D. Roper, C. Durney, and D. Christensen, "Modeling sources in the FDTD formulation and their use in quantifying source and boundary condition errors," IEEE Trans. Microwave Theory and Techniques **43**(4), 810–814 (1995).

[15] R. Mehra, L. Antani, S. Kim, and D. Manocha, "Source and listener directivity for interactive wave-based sound propagation," IEEE Trans. Visualization Comp. Graphics **20**(4), 83–94 (2014).

[16] J. Hargreaves, L. Rendell, and Y. Lam, "A framework for auralization of boundary element method simulations including source and receiver directivity," J. Acoust. Soc. Am. **145**(4), 2625–2637 (2019).

[17] A. Southern and D. Murphy, "Low complexity directional sound sources for finite difference time domain room acoustic models," in *Proc. 126th Audio Eng. Soc. Conv.*, Munich, Germany (2009).

[18] J. Escolano, J. Lopez, and B. Pueo, "Directive sources in acoustic discrete-time domain simulations based on directivity diagrams," JASA Express Lett. **121**, 256–262 (2007).

[19] H. Hacihabiboglu, B. Günel, and A. Kondoz, "Time-domain simulation of directive sources in 3-d digital waveguide mesh-based acoustical models," IEEE Trans. Audio Speech Lang. Proces. **16**(5), 934–946 (2008).

[20] D. Takeuchi, K. Yatabe, and Y. Oikawa, "Source directivity approximation for finite-difference time-domain simulation by estimating initial value," J. Acoust. Soc. Am. **145**(4), 2638–2649 (2019).

[21] S. Bilbao, J. Ahrens, and B. Hamilton, "Incorporating source directivity in wave-based virtual acoustics: Time-domain models and fitting to measured data," J. Acoust. Soc. Am. **146**(4), 2692–2703 (2019).

[22] S. Bilbao, A. Politis, and B. Hamilton, "Local time-domain spherical harmonic spatial encoding for wave-based acoustic simulation," IEEE Signal Proces. Lett. **26**(4), 617–621 (2019).

[23] I. Hallaj and R. Cleveland, "FDTD simulation of finite-amplitude pressure and temperature fields for biomedical ultrasound," J. Acoust. Soc. Am. **105**(5), L7–L12 (1999).

[24] E. Martin, Y. Ling, and B. Treeby, "Simulating focused ultrasound transducers using discrete sources on regular Cartesian grids," IEEE Trans. Ultrasonics Ferroelectrics and Frequency Control **63**(10), 1535–1542 (2016).

[25] J. Robertson, B. Cox, J. Jaros, and B. Treeby, "Accurate simulation of transcranial ultrasound propagation for ultrasonic neuromodulation and stimulation," J. Acoust. Soc. Am. **141**(3), 1726–1738 (2017).

[26] E. Wise, B. Cox, J. Jaros, and B. Treeby, "Representing arbitrary acoustic source and sensor distributions in Fourier collocation methods," J. Acoust. Soc. Am. **146**(1), 278–288 (2019).

[27] B. Treeby, J. Budisky, E. Wise, J. Jaros, and B. Cox, "Rapid calculation of acoustic fields from arbitrary continuous-wave sources," J. Acoust. Soc. Am. **143**(1), 529–537 (2018).

[28] R. Troian, D. Dragna, C. Bailly, and M.-A. Galland, "Broadband liner impedance eduction for multimodal acoustic propagation in the presence of a mean flow," J. Sound Vib. **392**(1), 200–216 (2017).

[29] E. Heyman and A. Devaney, "Time-dependent multipoles and their application for radiation from volume source distributions," J. Math. Phys. **37**(2), 682–692 (1987).

[30] P. Croaker, S. Marburg, R. Kinns, and N. Kessissoglou, "Multipole moment preserving condensation of volumetric acoustic sources," in *Proceedings of Acoustics 2011*, Gold Coast, Australia (2011).

[31] A. Pierce, *Acoustics: An Introduction to its Physical Principles and Applications* (Acoustical Society of America, Melville, New York, 1989), p. 162.

[32] E. Williams, *Fourier Acoustics: Sound Radiation and Nearfield Acoustical Holography* (Academic Press, New York, 1999), p. 2.

[33] B. Rafaely, *Fundamentals of Spherical Array Processing* (Springer, New York, 2015), p. 46.

[34] J. Ahrens, *Analytic Methods of Sound Field Synthesis* (Springer, Heidelberg, Germany, 2012), p. 30.

[35] J. Ivanic and K. Ruedenberg, "Rotation matrices for real spherical harmonics. direct determination by recursion," Journal of Physical Chemistry **100**(15), 6342–6347 (1996).

[36] J. Tuomela, "On the construction of arbitrary order schemes for the many-dimensional wave equation," BIT **36**(1), 158–165 (1996).

[37] S. Bilbao and B. Hamilton, "Higher-order accurate two-step finite difference schemes for the many dimensional wave equation," J. Comp. Phys. **367**, 134–165 (2018).

[38] E. Wise, B. Cox, and B. Treeby, "Staircase-free acoustic sources for grid-based models of wave propagation," in *IEEE International Ultrasonics Symposium*, Washington D.C. (2017).

[39] S. Bilbao and B. Hamilton, "Directional sources in wave-based acoustic simulation," IEEE Trans. Audio Speech Language Proces. **27**, 415–428 (2019).

[40] J. Waldén, "On the approximation of singular source terms in differential equations," Numerical Methods for Partial Differential Equations **15**(4), 503–520 (1999).

[41] X. Yang, X. Zhang, Z. Li, and G. He, "A smoothing technique for discrete delta functions with application to immersed boundary method in moving boundary simulations," J. Comp. Phys. **228**, 7821–7836 (2009).

[42] B. Hosseini, N. Nigam, and J. Stockie, "On regularizations of the Dirac delta distribution," J. Comp. Phys. **305**, 423–447 (2016).

[43] J. Saarelma, J. Botts, B. Hamilton, and L. Savioja, "Audibility of dispersion error in room acoustic finite-difference time-domain simulation as a function of simulation distance," J. Acoust. Soc. Am. **139**(4), 1822–1832 (2016).

[44] J. Meyer, T. Lokki, and J. Ahrens, "Identification of virtual receiver array geometries that minimize audibility of numerical dispersion in binaural auralizations of finite difference time domain simulations," in *149th Audio Engineering Society Convention paper*, New York (2020).